INVESTIGATION OF THE LOW-REYNOLDS NUMBER FLOW AROUND A FLAPPING FLEXIBLE AIRFOIL

Ralf Unger⋆, Matthias C. Haupt⋆ and Peter Horst⋆

⋆Institute of Aircraft Design and Lightweight Structures,
Technische Universität Braunschweig
Hermann-Blenk-Str. 35
38108 Braunschweig, Germany
r.unger, m.haupt, p.horst@tu-braunschweig.de

Key words: Flapping flight, Low-Reynolds number flow, Laminar-turbulent transition, Laminar separation bubble, Fluid-Structure interaction, Aeroelasticity

Abstract. *In this paper, a coupling simulation methodology is applied to investigate the fluid flow around a light and flexible airfoil based on a handfoil of a seagull. A finite element model of the flexible airfoil is fully coupled to the flow solver by using a load and displacement transfer as well as a fluid grid deformation algorithm. The flow field is characterized by a laminar-turbulent transition at a Reynolds number of Re=100000, which takes place along a laminar separation bubble. An unsteady Reynolds-averaged Navier-Stokes flow solver is used to take this transition process into account by comparison of a critical N-factor with the N-factor computed by the e^N-method. Results of computations have shown that the flexibility of the airfoil has a major influence on the thrust efficiency, the mean drag and lift, and the location of laminar-turbulent transition. The thrust efficiency can be considerably improved by increasing the plunging amplitude and by using a time dependent airfoil stiffness, inspired by the muscle contraction of birds.*

1 INTRODUCTION

The development of micro aerial vehicles with flapping wing propulsion and with its broad range of application is a recent research field [1, 2, 3]. The flapping wing concept inspired by bird's locomotion is promising for reaching high a propulsive efficiency. In the context of the flapping flight motion, both necessary flight forces - lift and thrust - are generated by pitching-plunging mechanism in conjunction with a low-Reynolds number flow regime. Here, for simplification a two-dimensional airfoil is investigated first and the question arises, if flexibility of such an airfoil is advantageous for the propulsion efficiency. In this paper this issue is addressed. Further, the aerodynamic behavior of the flapping wing propulsion is still not adequately understood and needs to be investigated. In [4], a flexible flat-plate connected to a stiff tear-drop like airfoil was experimentally investigated at low-Reynolds numbers and the flexibility of the plate was responsible for improvements of the airfoil propulsive efficiency.

However, the accurate prediction of the flow behavior using computational fluid dynamics (CFD) is still challenging due to the occurrence of a laminar-turbulent transition [5, 6, 7, 3]. This transition takes place along a laminar separation bubble, which is caused by a strong adverse pressure gradient within the laminar boundary layer and along the smooth aerodynamic surface. The evolution of the flow from laminar to turbulent proceeds in three stages [6]. In the first, receptivity stage, external disturbances like free stream turbulence or acoustic waves are transformed into low disturbances with wave characteristics within the boundary layer. In the second stage, a small number of unstable waves (Tollmien-Schlichting waves) are amplified and grow exponentially. Their behavior can be mathematically described by the linear stability theory [8]. In the third stage, the amplitudes of the waves increase and a nonlinear interaction with the boundary layer occurs. Thereby, the mean boundary layer profile distorts and the laminar boundary layer breaks down to turbulence.

For the simulation of such flow phenomena fully coupled with a flexible thin structure, a high qualitative and time resolved coupling schemes nowadays used for fluid-structure interaction problems is utilized [9]. The so-called partitioned coupling approach uses well-validated fluid as well as structural solvers, which are linked together within a simulation environment by the aid of flexible data transfer libraries [10]. For the structure itself, a nonlinear finite element methodology is applied [11, 12]. The first eigenfrequency of the structural model is validated against the designed model for the wind tunnel test campaigns [13]. For the fluid part of the simulation environment, an unsteady Reynolds-averaged Navier-Stokes (URANS) flow solver [14] is modified to take the transition process into account [7]. Thus, for the second stage of the transition process, the linear stability solver LILO [15] is directly coupled to the flow solver to investigate the flow field and especially the boundary layer of the airfoil. The transition location on the upper and lower side of the airfoil is calculated by comparison of a critical N-factor to the N-factor computed by the e^N-method [16, 17]. Due to the use of a URANS solver the first stage is empirically considered by a calibration of the critical N-factor. Further it is assumed that the third stage is very short and that therefore the location of the breakdown to turbulence is equal to the end of the second stage [6].

In this paper, the simulation environment is applied to a flexible airfoil and numerical flow computations are presented, where parameters are varied to improve the propulsive efficiency of the flapping airfoil motion. Thus, the remainder of the paper is organized as follows. In

section 2, the used fluid solver and the coupling environment are introduced. The calculation of the structural jig-shape with the aid of the coupling simulation, which come along with steady state fluid solution will be presented in section 3. Validation of the coupled analysis with given experimental is the topic of section 4. In section 5, some parameter studies are accomplished to improve the propulsive efficiency of the flapping motion.

2 FLUID SOLVER AND COUPLING SCHEME

For the computation of the flexible airfoil interacting with an incompressible fluid at a low Reynolds number, the Navier-Stokes solver FLOWer is integrated into the flexible coupling environment *ifls* . To calculate the transition location along the airfoil, the velocity profiles from the URANS solution are treated with a linear stability solver, which provides the amplification rates of the instability. These amplification rates are used to predict the transition location by comparison with a critical N-factor.

2.1 Description of the fluid solver with transition prediction

The unsteady Reynolds averaged Navier-Stokes equation (URANS) are calculated by the flow solver FLOWer, [14], which uses block-structured grids in conjunction a finite volume spatial discretization scheme. Here, a cell-centered scheme is utilized and the convective fluxes across the cell edges are treated with a second order-accurate central differencing scheme with scalar dissipation. The fluid solution is iterated to steady state by a five stage multigrid scheme. The true transient solution is recovered with the aid of second order accurate implicit dual-time stepping approach. Menter's baseline (BSL) turbulence model is used on a single grid basis. Acceleration of convergence is accomplished by a local time stepping, residual smoothing and multigrid. A low-Mach number preconditioning is used to improve accuracy. Because the fluid grid changes in every time step due to the grid deformation, the ALE form of the Navier-Stokes equation is solved and the geometric conservation law (GCL) is satisfies within the flow solver.

To calculate the amplification rates, the linear stability equation solver LiLO is used. The laminar boundary layer is transferred to this solver and the harmonic-wave assumption is applied to the primary flow variables velocity $\boldsymbol{v}_f$ and pressure p_f. LiLO solves the temporal stability problem for the wave mode of the primary flow variables to obtain the complex eigenvalue, [15, 18]. This eigenvalue calculation is efficiently performed by an inverse Rayleigh iteration as well as fast searching methods, [18].

Finally, the transition location is obtained by calculating the N-factor distribution for each frequency of an amplified mode. The N-factor curve is obtained by taking the envelope of all N-factor distributions. By comparison of this envelope with a critical N-factor, the location of transition is found. This e^N-method is motivated by the observation, that the location at which the boundary layer is developed to full turbulence corresponds with the amplification factor of the most unstable wave.

2.2 Coupling scheme

For a coupled problems like a fluid flow interacting with a flexible structure, a so-called two-field approach is used here, [19]. Both, the fluid and the structure, need to interchange data at an interface. In the context of the two-field approach the whole coupled problem can be written
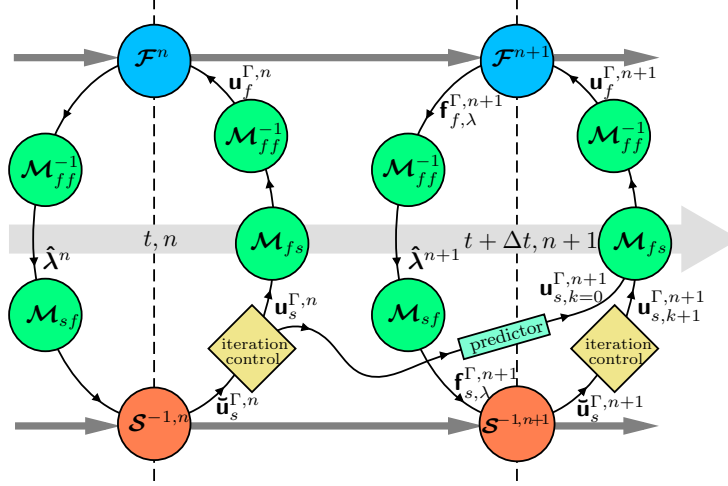
Figure 1: Time integration and equilibrium iteration for the coupled problem

in an operator-matrix form as:

$$
\begin{array}{c} \text{Fluid:} \\ \text{Structure:} \\ \text{State Transfer:} \end{array}
\left[\begin{array}{ccc} \mathcal{F} & 0 & -\mathcal{M}_{ff} \\ 0 & \mathcal{S} & \mathcal{M}_{sf} \\ -\mathcal{M}_{ff} & \mathcal{M}_{fs} & 0 \end{array}\right]
\left[\begin{array}{c} \mathbf{u}_f^\Gamma \\ \mathbf{u}_s^\Gamma \\ \hat{\boldsymbol{\lambda}} \end{array}\right]
=
\left[\begin{array}{c} \mathbf{0} \\ \mathbf{f}_s^\Gamma \\ \mathbf{0} \end{array}\right]
\tag{1}
$$

where the fluid and structural operators $\mathcal{F}$ and $\mathcal{S}$ involve the computations of the fluid and structure subdomain, respectively. The nodal vectors $\mathbf{u}_f^\Gamma$ and $\mathbf{u}_s^\Gamma$ denotes the displacement field vectors on the fluid (subscript: $_f$) and structural (subscript: $_s$) interface Γ, respectively. The vector $\hat{\boldsymbol{\lambda}}$ is the vector of discrete Lagrange multipliers, which links the fluid and structure together. The Lagrange multiplier is defined on the fluid interface representation, to make the above system solveable. The vector $\mathbf{f}_s^\Gamma$ is the external nodal forces on the structure, which have other sources than the forces caused aerodynamically by the fluid. The coupling matrices are calculated by an integral statement as:

$$
\mathcal{M}_{ij} = \int\limits_\Gamma \mathbf{N}_i^T \mathbf{N}_j \, d\Gamma \,,
\tag{2}
$$

where $\mathbf{N}_i$ are the shape functions of the interface discretization i. Without access to the matrices of each solver $\mathcal{S}$ or $\mathcal{F}$ the classical Richardson iteration can be used to find a solution of the system:

$$
\mathbf{u}_{s,k+1}^\Gamma = \varsigma_{RI} \underbrace{\mathcal{S}^{-1} \circ (\mathbf{f}_s^\Gamma - \mathcal{M}_{sf} \circ \mathcal{M}_{ff}^{-1} \circ \mathcal{F} \circ \mathcal{M}_{ff}^{-1} \circ \mathcal{M}_{fs} \circ \mathbf{u}_{s,k}^\Gamma)}_{\breve{\mathbf{u}}_{s,k+1}^\Gamma} + (1 - \varsigma_{RI})\mathbf{u}_{s,k}^\Gamma
\tag{3}
$$

where ς_{RI} is the user defined relaxation parameter for the Richardson iteration. In each iteration a Dirichlet-Neumann step, $\mathcal{F}$-$\mathcal{S}^{-1}$ is invoked to get the displacement field of the fluid and structure on the interface, respectively.

4
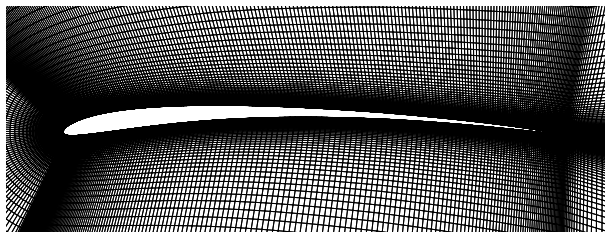
Figure 2: close-up view on the structured grid for flow calculation over the SG04 airfoil

Here, simple staggered scheme is used, with implies $\varsigma_{RI} = 1.0$ and $k_{max} = 1$. With this iteration procedure, the time integration and equilibrium iteration of the coupled problem can be illustrated as shown in Figure 1, where the time loop index is n and the iteration index is k. For the vector $\mathbf{u}_{s,k=0}^{\Gamma,n+1}$ a second order time accurate predictor is used based on the structural forces obtained in the previous time step, [20]. Within the iteration control box a relaxation of the most recent computed structural displacement field $\bar{\mathbf{u}}_s^{\Gamma,n+1}$ is conducted.

3 STATIONARY SOLUTION AND CALCULATION OF THE JIG-SHAPE

A steady computation was utilized to calculate the jig-shape of the structural model, which is needed for the design of the wind tunnel model. The jig-shape is the shape of the airfoil that is not affected by any inertial or aerodynamic forces, i.e. the shape of the airfoil in rest without fluid flow around it. To obtain the aerodynamic shape of the original aerodynamic airfoil, a gliding flight with a Reynolds number of $Re = 10^5$ and angle of attack $\alpha = 3°$ is assumed. The structured grid used for this calculation consists of 585x129 nodes and is partially shown in Figure 2. To get the jig-shape of the airfoil, an iteration process similar to the Richardson iteration is carried out, where the residual is taken as the difference to the original SG04 airfoil.

In Figure 3(a) the jig-shape is depicted as the black boundary line. The pressure distribution of the fluid flow around the airfoil is also seen in this figure and the pressure distribution on the airfoil surface is depicted in Figure 3(b). The displacement at the trailing edge is calculated to 3.5% of the chord length l_c. The location of the transition on the upper side of the airfoil is calculated to be at $x_t/l_c = 0.66$. This also can be seen from Figure 3(b), where the transition point is indicated by the strong pressure rise on the upper surface at this location. The resulting turbulent reattachment occurs at a location 71% of the chord length. The dimensionless velocity contours are shown in Figure 3(c) together with streamlines indicating the laminar separation bubble. The corresponding $\overline{v_1' v_3'}$ contours are shown in Figure 3(d). The $\overline{v_1' v_3'}$ contours are chosen to be plotted because the turbulent shear stress $\tau_{13}^T = -\rho \overline{v_1' v_3'}$ causes transport of momentum across the boundary layer, which is responsible for the closure of the laminar separation bubble. The calculations were carried out with a critical N-factor of $N_{\text{crit}} = 8$, which corresponds to a turbulence level of 0.1%.

4 VALIDATION OF THE COUPLED ANALYSIS

In this section, the coupled analysis of the flexible airfoil is validated with given experimental data, which are published in [21]. A testcase consisting of a combined pitching-plunging motion is chosen and this testcase is validated in terms of the structural deformation, transition location
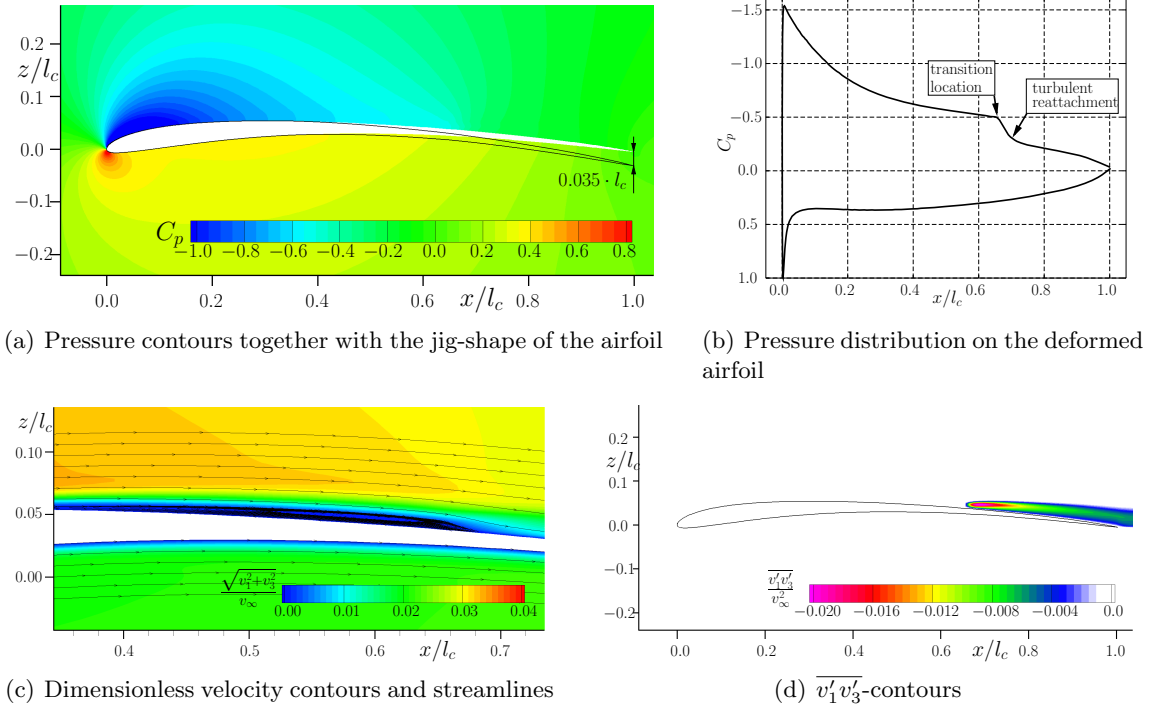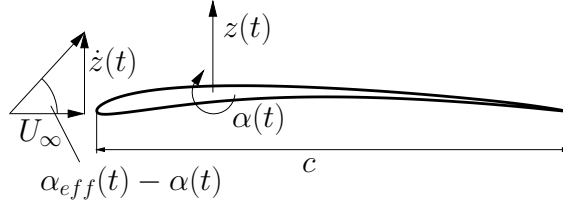
(a) Pressure contours together with the jig-shape of the airfoil

(b) Pressure distribution on the deformed airfoil

(c) Dimensionless velocity contours and streamlines

(d) $\overline{v_1' v_3'}$-contours

Figure 3: Analysis of the airfoil in gliding flight ($Re = 10^5$, $\alpha = 3°$)

Figure 4: Definition of the effective angle of attack

and the turbulent shear stress distribution around the airfoil.

4.1 Motion parameters

A harmonic pitching-plunging motion of the airfoil is investigated here for the flapping flight simulation. The plunging part of the motion with $z(t)$ being the position of the quarter-chord line can be expressed as:

$$z(t) = \hat{z} \cos(2\pi f t).$$ (4)

6
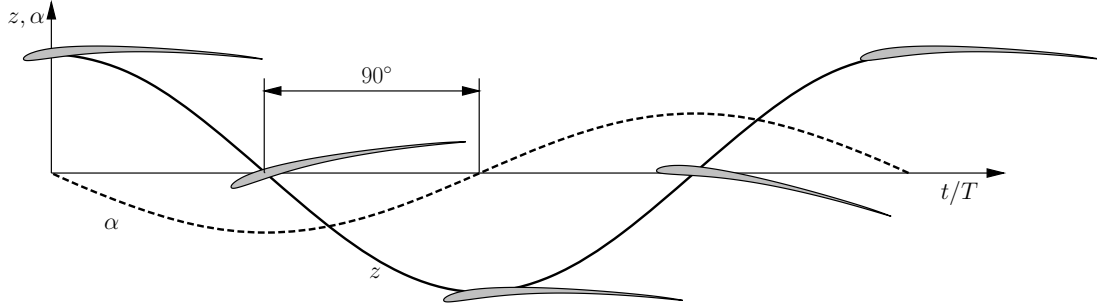
Figure 5: Combined pitch-plunge motion witch 90° phase shift

The effective angle of attack due to the pitching motion is then, see also Figure 4:

$$
\begin{aligned}
\alpha_{\text{eff}}(t) &= \alpha(t) + \arctan\left(\frac{-\dot{z}(t)}{U_\infty}\right) \\
&= \alpha_0 - \hat{\alpha}\sin(2\pi ft) + \arctan\left(\frac{2K\hat{z}}{c}\sin(2\pi ft)\right) \\
&\approx \alpha_0 + \left(\frac{2K\hat{z}}{c} - \hat{\alpha}\right)\cdot\sin(2\pi ft),
\end{aligned}
\tag{5}
$$

where the $K = \pi fc/U_\infty$ is the reduced frequency and a phase angle of 90° between the plunging and pitching motion is assumed. Such a phase shift is optimal corresponding to Küssner's theory [22] and observation of Lilienthal [23]. Here the following parameters for the flapping flight simulation are used:

- reduced frequency of $K = 0.2$

- plunging amplitude of $\hat{z} = 0.5c$

- angle of attack of $\alpha_0 = 4°$

- effective angle of attack amplitude of $\hat{\alpha}_{\text{eff}} = \frac{2K\hat{z}}{c} - \hat{\alpha} = 4°$

- Reynolds number of $Re = 10^5$

- time step size of $\Delta t = \frac{1}{500f}$

A sketch of this combined pitching-plunging motion is depicted in Figure 5.

The parameter of the physical system like motion parameters, structural parameters and fluid parameters are assessed through the lift and drag (or thrust) coefficient as well as the propulsive efficiency defined as:

$$
\eta = \frac{\frac{1}{TU_\infty}\int\limits_0^T \sum\limits_{n=1}^N U_\infty(c_{x,n} - c_{x,stat})\,dt}{\frac{1}{TU_\infty}\int\limits_0^T \sum\limits_{n=1}^N (c_{x,n}u_n + c_{y,n}v_n + c_{z,n}w_n)\,dt}
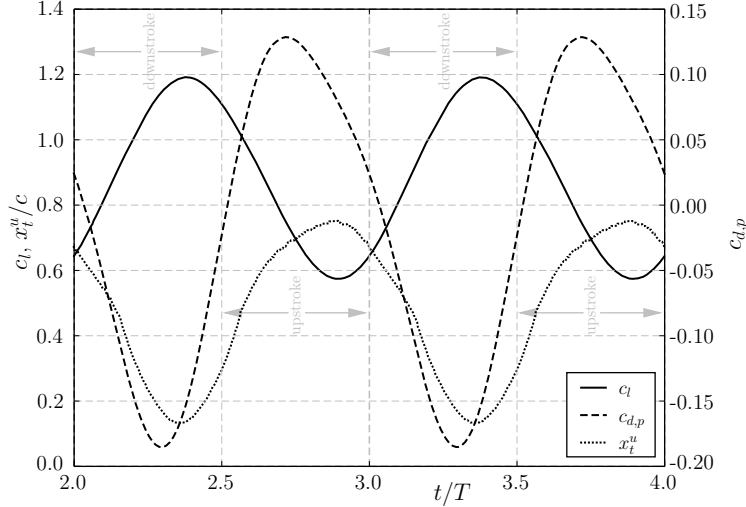\tag{6}
$$

Figure 6: Lift and drag due to pressure coefficients as well as transition location of the flapping flexible airfoil during two periods of motion

where $T = 1/f$ is the flapping period, N denotes the number of nodes on the airfoil surface. The values $(c_{x,n}, c_{y,n}, c_{z,n})$ are the force coefficient at the surface node n. Similarly, (u_n, v_n, w_n) are the nodal velocities. A correction $c_{x,stat}$ is used to compare the efficiency of the flapping flight motion with a propeller-driven device. The value of $c_{x,stat}$ is defined as the lowest drag coefficient of the flexible airfoil, which can be reached with steady state analyses at different angle of attacks.

4.2 Validation of the reference testcase

The resulting time history of the lift and pressure induced drag coefficient as well as the evolution of the transition location of the upper airfoil side is shown in Figure 6 for two periods of the motion. Here, it can be seen, that due to the unsteady fluid flow, the always positive lift has its maximum during the downstroke shortly after the mid-downstroke although the highest effective angle of attack is reached at $t/T = 0.25 + i$ (i being the period number). The mean lift over one period is $\bar{c}_l = 0.8802$. The highest negative drag, i.e. thrust, is also reached during the downstroke shortly after the mid-downstroke but before the maximum lift is obtained. On the other hand the highest positive drag is obtained shortly before the mid-upstroke. Integrating the drag over one period gives the mean drag, which is computed as $\bar{c}_{d,p} = -0.0128$, i.e. thrust is generated during one flapping period. The propulsive efficiency is calculated to $\eta = 0.827$. From the time history plot of the transition location, it can be observed, that the laminar separation bubble moves from the trailing edge towards the leading edge during the downstroke and moves back during the upstroke, while it never reaches the last 30% of the rear part. Thus, the laminar separation bubble is present all time for the flapping flexible airfoil. The lowest reached transition location is obtained at $t/T = 0.35 + i$ with a value of $x_t^u/c = 0.134$. The effect of this laminar separation bubble to the pressure distribution of the upper side of the airfoil is shown in Figure 7, where the c_p-value is plotted over the $x/c - t/T$-plane for one period and
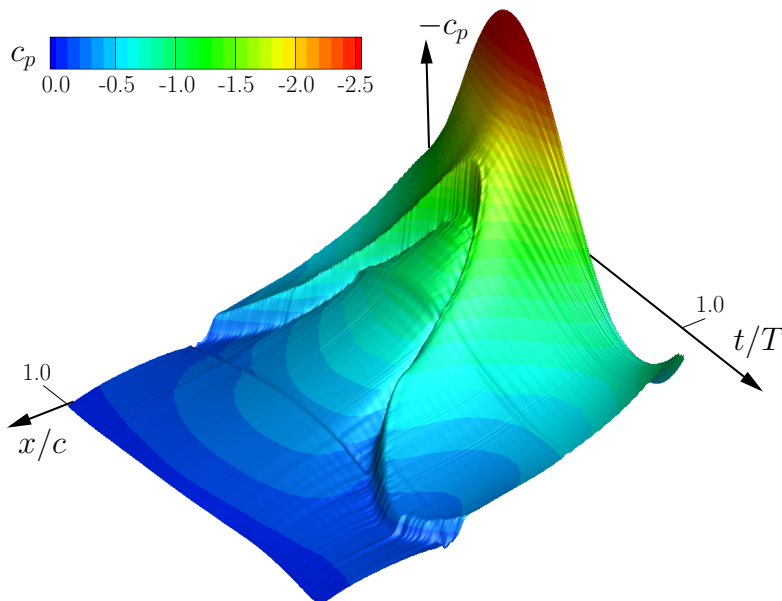
8

Figure 7: Pressure distribution of the upper airfoil over one period

also colored. As already noticed in Figure 3(b), a jump in the c_p distribution is induced due to laminar-turbulent transition. This jump moves together with transition location from the trailing to the leading edge during one period of motion, where the height of the jump increases with lower values of x_t^u/c.

The turbulent shear stress distribution, which is an adequate indicator for the transition from laminar to turbulent flow, is shown in Figure 8 for four discrete time points together with the turbulent shear stress obtained in wind tunnel test campaigns, published in [21]. These experimental data were obtained with the aid of stereoscopic PIV measurements at the flapping airfoil, where the flow velocity was captured at several window locations around the airfoil and at multiple time instances. These sets of velocity vector images is ensemble averaged to get the desired turbulent stress. From the comparison it can be observed, that at the top dead center the computed transition location is more upstream than that found in the experiment, Figure 8(a). This situation changes during the downstroke and at the mid-downstroke the calculated transition location lies behind the experimental found location, Figure 8(b). This indicates, that the change of x_t^u is insufficiently resolved by the numerical scheme. During the upstroke the experimental found transition location is again more downstream than numerical predicted, Figure 8(c) and 8(d). This disagreement was already noticed for the rigid version of the airfoil and is likely caused by the turbulence assumption of the URANS solver, [21].

Finally, the trailing edge deformation during one period of flapping motion is shown in Figure 9. Here, the data obtained from the computation are compared with experimental data, which are measured with the aid of an optical 3D deformation system. This system uses a stochastic pattern on the specimen's surface captured by two CCD cameras and a cross correlation scheme to calculate the deformation. The highest deformation is numerically obtained shortly after the top dead center at $t/T = 0.1$, while the experiment predicts the highest de-

(a) at time $t/T = 0$ (top dead center)

(b) at time $t/T = 0.25$ (mid-downstroke)

(c) at time $t/T = 0.625$ (upstroke)
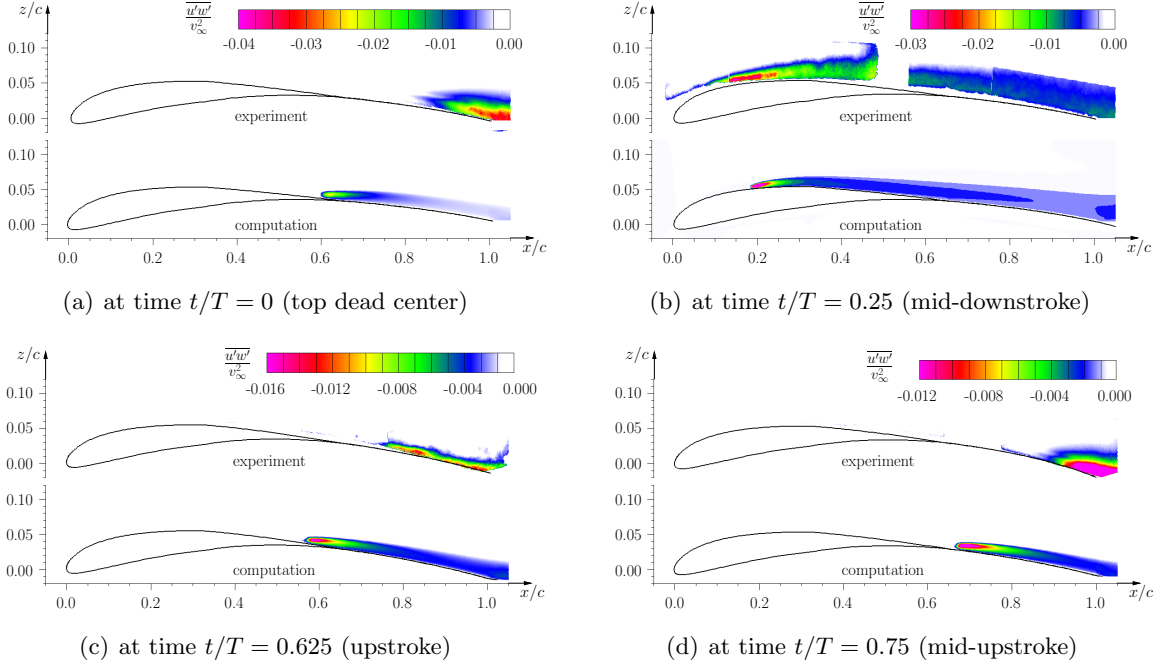
(d) at time $t/T = 0.75$ (mid-upstroke)

Figure 8: Comparison of computational and experimental results in terms of the turbulent shear stress distribution around the airfoil at several time instances - experimental data from [21]

formation closer to the top dead center. The deformation decreases, i.e. the camber increase, while the airfoil moves to the bottom dead center. This behavior is principal indentical for both, the computation and the experiment, although the computation predicts higher deformation at the bottom dead center. This discrepancy has three sources: firstly, with the deformation measuring system it is impossible to resolve exactly the trailing edge deformation due the use of uniform voxels in which the obtained images are resolved. Secondly and a more important source is the accuracy of the model's jig-shape. Due to the used orthotropic material for the curved shells, structure manufacture related initial stresses are unavoidable for the wind tunnel model, which results in spanwise distortion. The deviation of the vertical trailing edge position due to the curvature of the structural model is temperature dependent and is about 1.0 - 1.5 mm in spanwise direction. This is even intensified due to the anticlastic deformation of the trailing edge, which is non-neglectable due to the geometry of the manufactured model (the span is double of the chord). A third source of the discrepancy is the presence of the wind tunnel walls, which are not modeled in the computations.

5 PARAMETER STUDIES

With the validated computational simulator, different parameter studies can now be conducted. Based on the reference testcase, some parameters were varied, to study the influence on the propulsive efficiency.
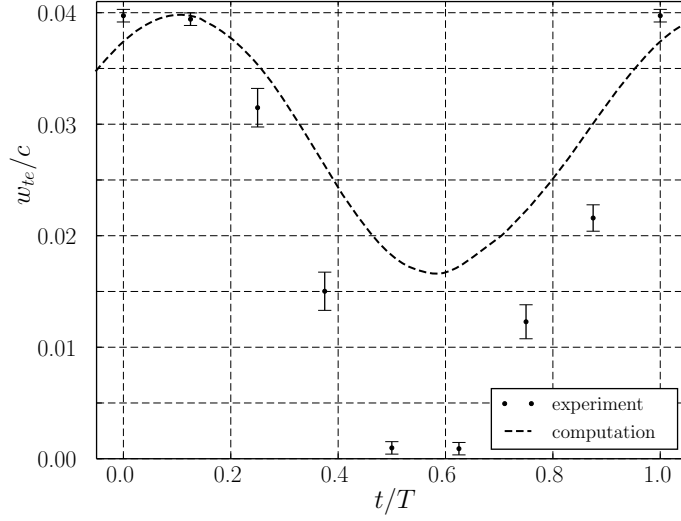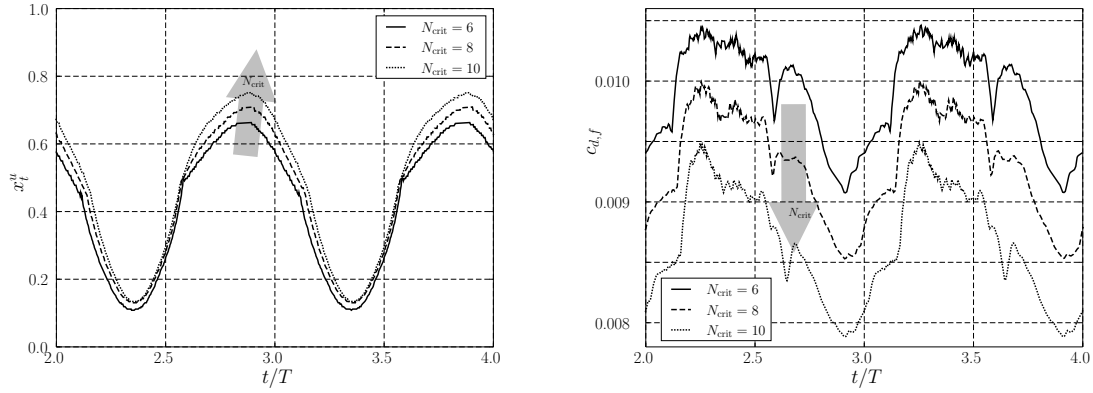
Figure 9: Trailing edge deformation during one period of motion - comparison of numerical and experimental data

(a) transition location of the upper airfoil over two periods of the flapping motion

(b) friction induced drag over two periods of the flapping motion

Figure 10: Transition location and friction induced drag over two periods of the flapping motion at different critical N-factors

	critical N-factor		
	$N_{\mathrm{crit}} = 6$	$N_{\mathrm{crit}} = 8$	$N_{\mathrm{crit}} = 10$
propulsive efficiency η:	0.808	0.827	0.835

Table 1: Propulsive efficiency at different critical N-factors

5.1 Influence of the critical N-factor N_{crit}

Initially, the critical N-factor N_{crit} was varied to investigate the influence of the turbulence level of the wind tunnel, i.e. to verify if the wind tunnel has a major influence on the mean lift, drag or propulsive efficiency. In the previous calculations a critical N-factor of $N_{\mathrm{crit}} = 8$ was assumed. It could be observed, that with increasing the critical N-factor N_{crit} the laminar separation bubble moves more to the trailing edge, which results in an offset of the transition location, Figure 10(a). This offset is more distinctive, when the LSB is closer to the trailing edge. With the change of the transition location also an offset in the time history of the friction induced drag could be noticed, Figure 10(b). Increasing the critical N-factor, the friction induced drag is decreased. Since the influence of N_{crit} to the lift and the pressure induced drag is marginal, the propulsive efficiency is slightly improved, Table 1.

5.2 Influence of the plunging amplitude $\hat{z}$

A major influence on the aerodynamic coefficients is given through the plunging amplitude $\hat{z}$. Here, the plunging amplitude is defined by an angle amplitude as $\hat{\zeta} = \frac{2K\hat{z}}{c}$, while keeping the effective angle of attack constant, i.e. $\hat{\alpha}_{\mathrm{eff}} = \hat{\zeta} - \hat{\alpha} = 4° = \mathrm{const.}$. Further, it is useful to define an amplitude ratio as:

$$r_{\hat{\alpha}\hat{\zeta}} = \frac{\hat{\alpha}}{\hat{\zeta}} = \frac{\hat{\alpha}c}{2K\hat{z}} \,. \tag{7}$$

The testcase given above has an angle amplitude of $\hat{\zeta} = 11.4°$ and an amplitude ratio of $r_{\hat{\alpha}\hat{\zeta}} = 0.65$.

In Figure 11(a), the lift coefficient over two periods of the flapping motion is plotted. It can be seen, that with increasing the plunging amplitude $\hat{\zeta}$ (with keeping $\hat{\alpha}_{\mathrm{eff}} = \mathrm{const.}$), the highest lift is also increased, while the time point where the highest lift occurs becomes closer to the bottom dead center. The lowest lift value is additionally reduced with higher values of $\hat{\zeta}$ and also shifted but to the top dead center. However, with $\hat{\zeta} = 25°$, separation occurs at the leading edge and the computation becomes unstable. Such a shift cannot be observed in the time history of pressure induced drag, Figure 11(b). Nevertheless, with higher values of $\hat{\zeta}$ the thrust (negative drag) and positive drag is increased during the downstroke and upstroke, respectively. Integrating $c_{d,p}$ over one period, one can see that the net thrust is increased until $\hat{\zeta} = 20°$, Figure 11(d). Accordingly, the propulsive efficiency is increased up to $\hat{\zeta} = 20°$, but this enhancement is limited due to the occurrence of the leading edge vorticities, Figure 11(d). Finally, the evolution of upper airfoil transition location is shown in Figure 11(c). The amplitude of the transition movement is decreased with higher values of $\hat{\zeta}$ and also a phase shift with increased angle amplitudes can be observed here as it was already seen in the lift time history.

5.3 Influence of the flapping frequency

A further parameter, which obviously has a major influence is the flapping frequency, which is here expressed through the reduced frequency K. Additionally to the testcase described above, another testcase was chosen with $K = 0.4$ whereas the remaining parameters were kept constant, i.e. $\hat{\zeta} = 11.4°$ and $\hat{\alpha}_{\mathrm{eff}} = 4°$.
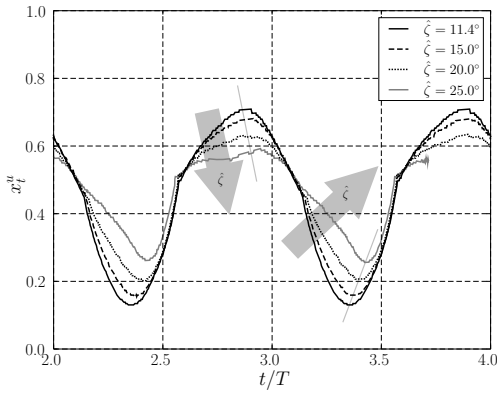
In Figure 12, the lift and drag coefficient due to pressure as well as the trailing edge deforma-
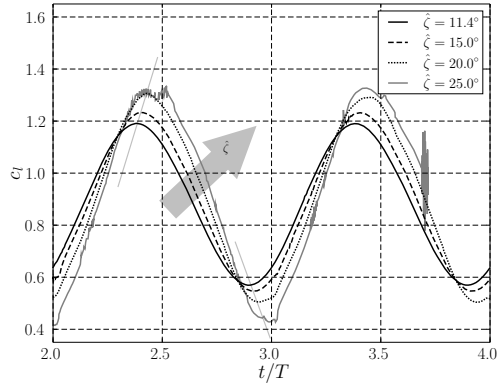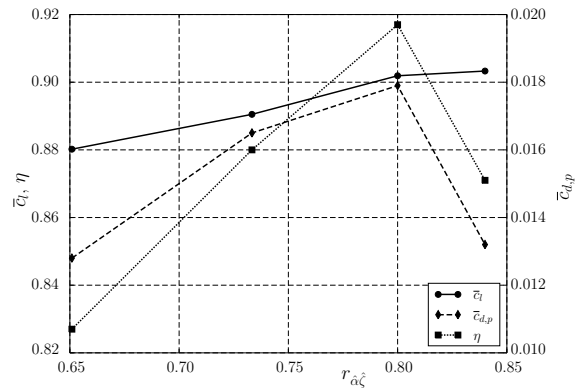
(a) lift coefficient over two periods of the flapping motion
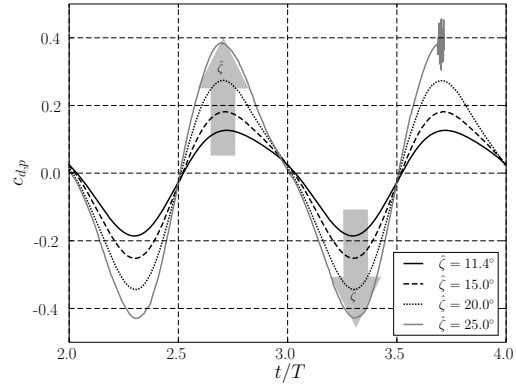
(b) pressure induced drag over two periods of the flapping motion

(c) transition location of the upper airfoil over two periods of the flapping motion

(d) development of the mean lift, pressure induced drag and propulsive efficiency with the amplitude ratio

Figure 11: Pressure induced drag, lift and transition location over two periods of the flapping motion at different plunging amplitudes

(a) lift coefficient and trailing edge deformation over two periods of the flapping motion

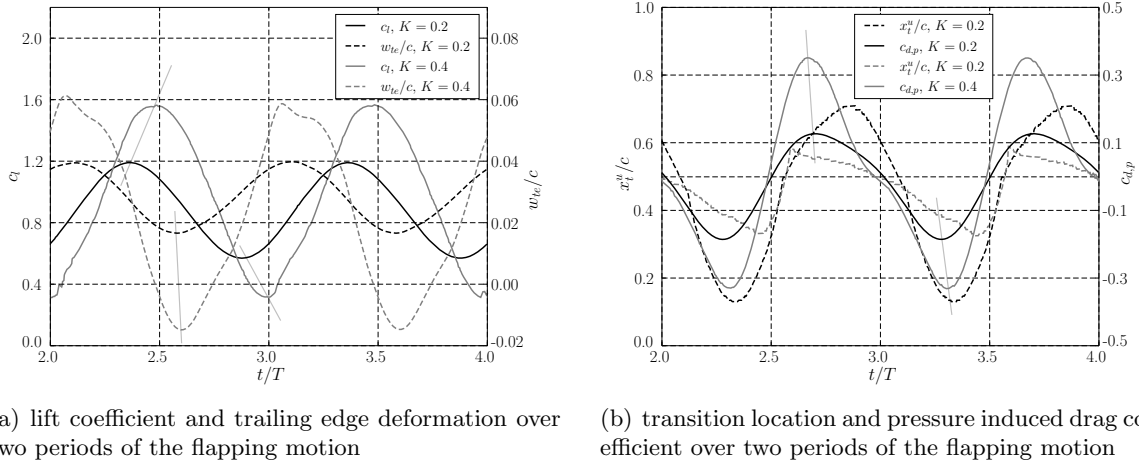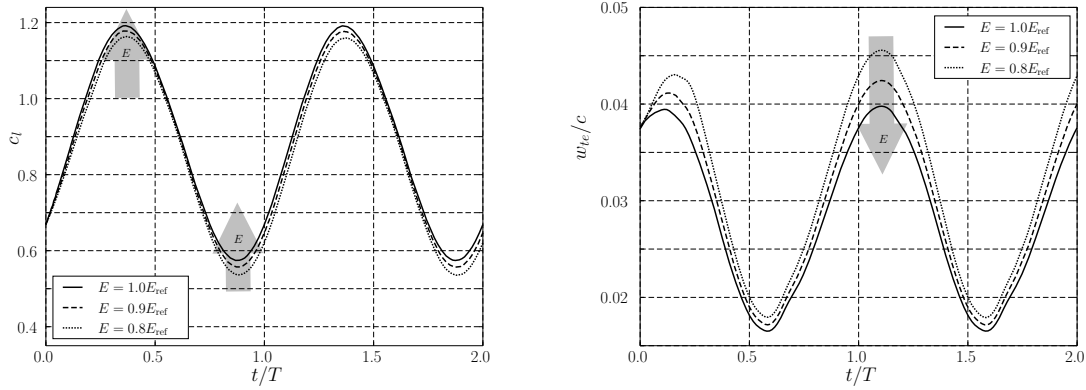(b) transition location and pressure induced drag coefficient over two periods of the flapping motion

Figure 12: Lift and trailing edge deformation as well as transition location and pressure induced drag coefficient over two periods of the flapping motion at two flapping frequencies

tion and the transition location of the upper airfoil are plotted over two flapping periods for the $K = (0.2, 0.4)$. Clearly, with a higher flapping frequency, also higher lift maxima and lower lift minima are obtained, Figure 12(a). However, the mean lift over one period is $\bar{c}_l = 0.974$, which is an increase of 11% compared to case with $K = 0.2$ Further, it can be seen here, that the highest and lowest lift value are now reached at the bottom and top dead center, respectively, i.e. a shift of the minimum and maximum lift values is observed. Such a strong shift could not be noticed for the trailing edge deformation evolution, Figure 12(a), which indicates that the lift shift is mainly caused by unsteady effects of the fluid flow. Also from Figure 12(a) it can be seen, that a higher structural mode appears is the trailing edge deformation time history.

A comparison of the transition location time histories at the two different flapping frequency is depicted in Figure 12(b). Here it can be seen, that the transition location is between $0.33 \leq x_t^u \leq 0.59$, i.e. the bandwidth in terms of the transition location is reduced. Further, it can be noticed from Figure 12(b), that the transition location is at the center of the upper airfoil chord and then moves slowly upstream. Shortly before the airfoil reaches the bottom dead center, the transition location jumps rapidly downstream to its maximum value before it then again moves slowly in upstream direction. In addition, the time history of the pressure induced drag is depicted in Figure 12(b). More thrust during the downstroke can be produced with $K = 0.4$, but also the drag is increased during the upstroke. A strong phase shift as it was observed at the lift coefficient when increasing the flapping frequency could not be observed in terms of the value $c_{d,p}$. The mean drag could be integrated to $\bar{c}_{d,p} = 0.0044$ for one period, i.e. no net thrust is generated with this configuration.

5.4 Influence of the airfoil stiffness

The influence of the airfoil stiffness is investigated in further computations. The stiffness can be varied by different methods, e.g. Young's modulus, thickness of the flexible shells the airfoil is made of. Additionally, the shells can be designed such that the thickness is tapered along the airfoil chord length. The major influence is given in the lift coefficient, which is

(a) lift coefficient over two periods of the flapping motion

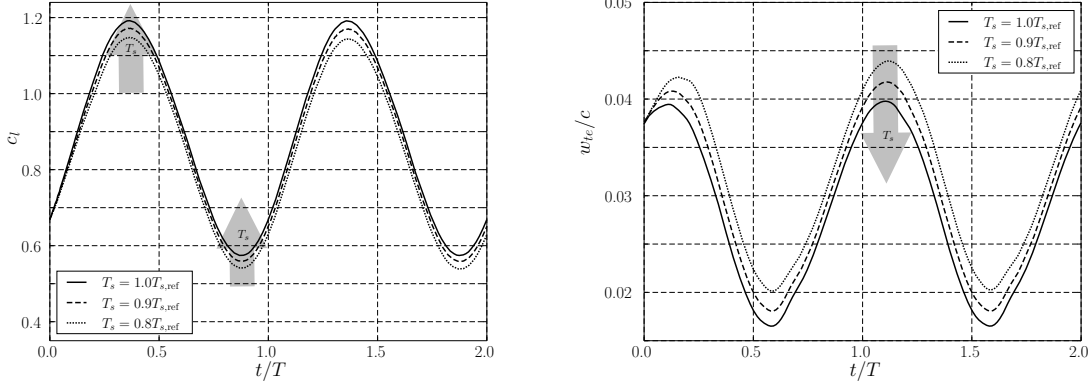(b) trailing edge deformation over two periods of the flapping motion

Figure 13: Lift and trailing edge deformation over two periods of the flapping motion at different airfoil stiffness

	Young's modulus E/E_{ref}		
	1.0	0.9	0.8
mean lift $\bar{c}_l$:	0.880	0.869	0.850
mean pressure induced drag $\bar{c}_{d,p}$:	-0.0128	-0.0117	-0.0115
propulsive efficiency η:	0.827	0.780	0.713

Table 2: Mean lift and drag and propulsive efficiency for different Young's modulus

shown in Figure 13(a), where Young's modulus is decreased compared to reference value E_{ref}. This stiffness reduction is done for the whole structural airfoil model. As one can see from Figure 13(a), a reduction of the stiffness (or increase of the flexibility) goes along with a decrease of the lift level over the whole flapping period. This reduction reaches a similar value at the time points, when the lift has its minimum and maximum value. Thus, the pressure induced drag/thrust and therefore the propulsive efficiency are reduced. The decrease of the efficiency is caused by the interaction of the aerodynamic forces and the deformation of the airfoil. Due to the reduction of the stiffness, the airfoil is more dewarped during the thrust producing downstroke, Figure 13(b), which results in a decrease of the aerodynamic force vector, which is directed towards the inflow vector. Indeed, the airfoil is also dewarped during the upstroke, Figure 13(b), but the additional trailing edge deformation is lower than that during the downstroke. This difference has a negative influence on the propulsive efficiency. The resulting mean lift and drag coefficients as well as the propulsive efficiency are summarized in Table 2.

The same expressions can be made, if varying the shell thickness. Such shells are used to create the flexible airfoil shape. In Figure 14, again the lift coefficients and trailing edge deformation over two periods are depicted. Accordingly to the stiffness variation, the lift is decreases with a reduction of the shell thickness over the whole flapping period. Further, with

(a) lift coefficient over two periods of the flapping motion

(b) trailing edge deformation over two periods of the flapping motion

Figure 14: Lift and trailing edge deformation over two periods of the flapping motion at different shell thicknesses of the airfoil

	shell thickness $T_s/T_{s,\mathrm{ref}}$		
	1.0	0.9	0.8
mean lift $\bar{c}_l$:	0.880	0.866	0.849
mean pressure induced drag $\bar{c}_{d,p}$:	-0.0128	-0.0117	-0.0117
propulsive efficiency η:	0.827	0.772	0.690

Table 3: Mean lift and drag and propulsive efficiency for different shell thicknesses of the airfoil

higher shell thicknesses, the trailing edge deflection is reduced, Figure 14(b). However, in this case the difference of the trailing edge deformation at its maxima compared to the deformation difference at its minimum is smaller as for the case, where Young's modulus was subject for variation. The resulting mean lift and drag coefficients as well as the propulsive efficiency are summarized in Table 3.

5.5 Temporal adaptive stiffness of the airfoil

The results from the previous section motivate to use a time dependent stiffness of the airfoil to increase the thrust during the downstroke and to decrease the drag during the upstroke. Thus, for the airfoil, a temporal adaptive stiffness is used, which can be described as:

$$E(t) = 0.5(E_{\max} - E_{\min})\sin(2\pi\, f\, t) + 0.5(E_{\max} + E_{\min})\,, \tag{8}$$

i.e. the airfoil becomes more stiff during the downstroke with the highest value of Young's modulus at the mid-downstroke and will be more flexible during the upstroke, where the minimal Young's modulus is reached at the mid-upstroke. Therefore, the dewarping of the airfoil during the downstroke is counteracted, whereas the dewarping is assisted during the upstroke. Initially,

(a) lift coefficient over one periods of the flapping motion

(b) pressure induced drag coefficient over one periods of the flapping motion

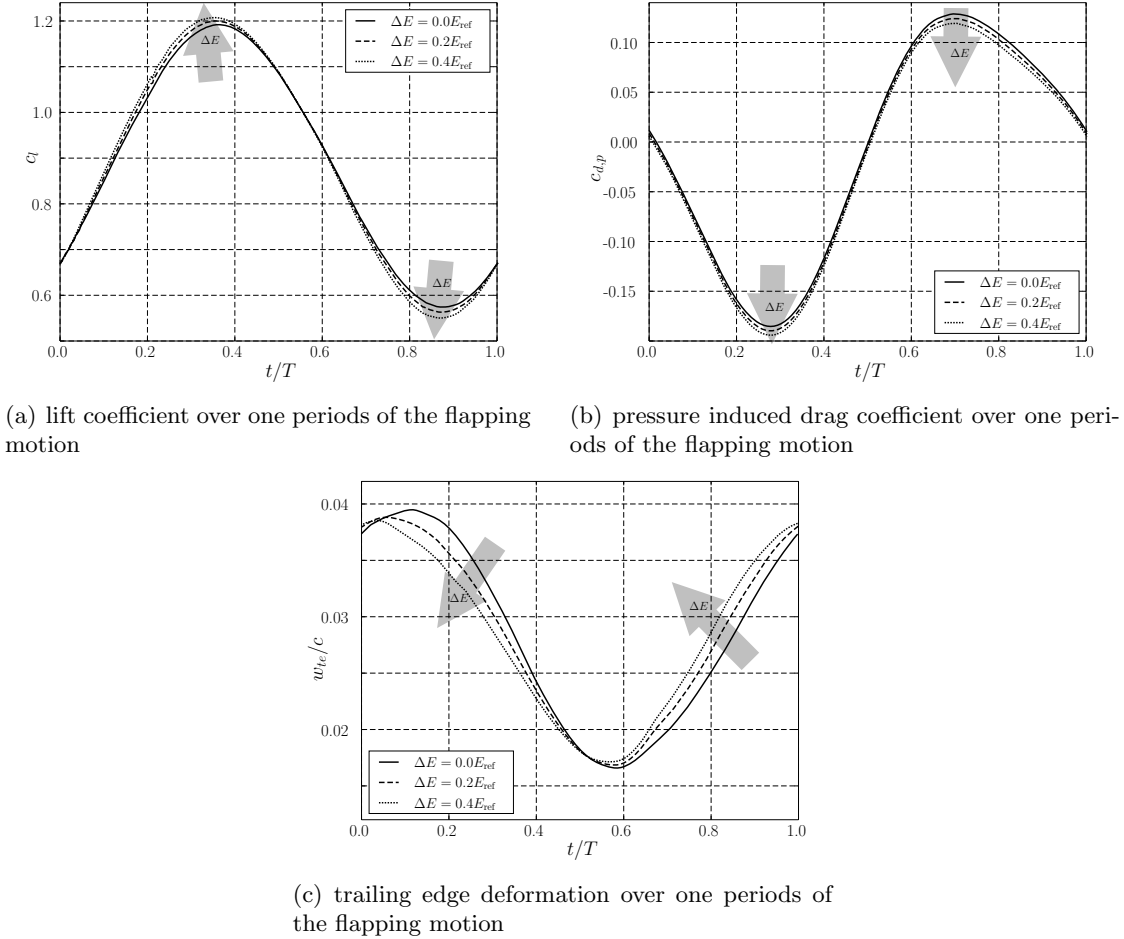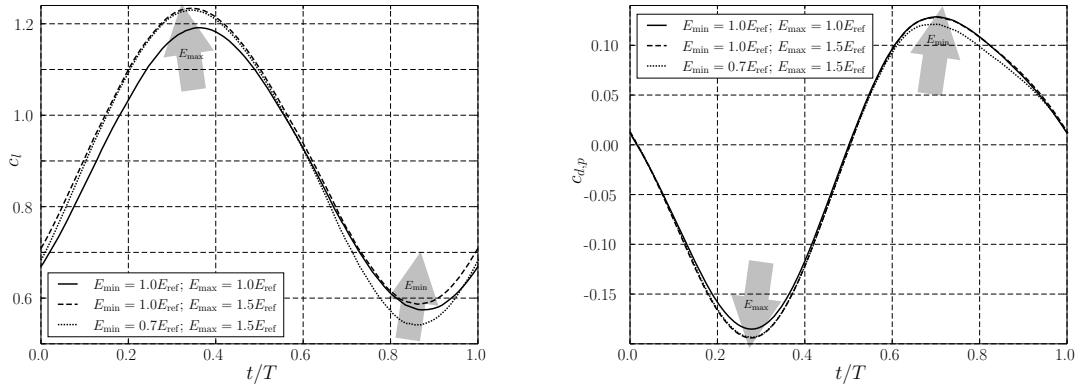(c) trailing edge deformation over one periods of the flapping motion

Figure 15: Lift, pressure induced drag and trailing edge deformation over one periods of the flapping motion at different amplitudes of Young's modulus

the mean value of Young's modulus is set to reference value, i.e. $0.5(E_{\max} + E_{\min}) = E_{\mathrm{ref}}$ and the amplitude $\Delta E = E_{\max} - E_{\min}$ is subject for variation.

In Figure 15 the lift, the pressure induced drag coefficients and the trailing edge deformation is plotted over the time for one period of the flapping motion. From Figure 15(a) it can be noticed, that the maximum lift is increased whereas the minimum lift is reduced with higher amplitudes of Young's modulus. Thus, the mean lift $\bar{c}_l$ is almost not affected by the time dependent airfoil stiffness, Table 4. For the pressure induced drag coefficient, it can be observed, that during the downstroke more thrust is generated due to the higher aerodynamic force vector, Figure 15(b). Likewise, less drag is produced during the upstroke due to the decreased aerodynamic force vector, which is directed downstream. In summary, this behavior leads to an improvement of the mean pressure induced drag, Table 4. Therefore, the propulsive efficiency is increased with higher stiffness amplitudes ΔE. Furthermore in Figure 15(c), the desired stiffening and flexibilization is seen in terms of the trailing edge deformation of the airfoil. During the downstroke the deformation is reduced, whereas for the upstroke the trailing edge shows a higher deformation.

	stiffness amplitude $\Delta E/E_{\mathrm{ref}}$		
	0.0	0.2	0.4
mean lift $\bar{c}_l$:	0.880	0.886	0.887
mean pressure induced drag $\bar{c}_{d,p}$:	-0.0128	-0.0130	-0.0132
propulsive efficiency η:	0.827	0.850	0.862

Table 4: Mean lift and drag and propulsive efficiency for different stiffness amplitudes ΔE

(a) lift coefficient over one periods of the flapping motion

(b) pressure induced drag coefficient over one periods of the flapping motion
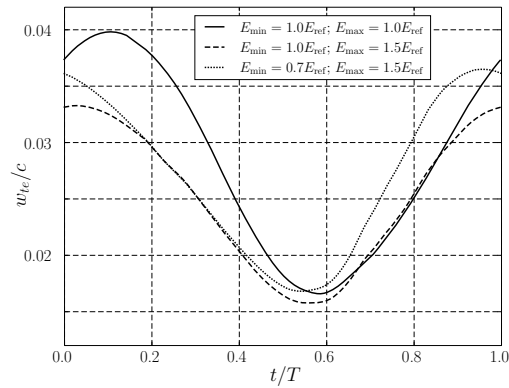
(c) trailing edge deformation over one periods of the flapping motion

Figure 16: Lift, pressure induced drag and trailing edge deformation over one periods of the flapping motion at different minima and maxima of Young's modulus

Finally, the influence of the minimum and maximum values of Young's modulus should be investigated. In Figure 16, the time histories of the lift, drag and trailing edge deformation is shown for further computations, where the lower bound of Young's modulus is subject to variation. In Figure 16(a), the lift evolution is seen and one can notice, that only the maximum value of Young's modulus is responsible for the highest peak in the lift, whereas E_{min} mainly influences the lowest peak of the lift. Similarly, only E_{max} is responsible for more thrust during the downstroke and the value of the minimum Young's modulus defines mainly the amount of drag during the upstroke, Figure 16(b). Surprisingly, such a correlation could not be noticed for the trailing edge deformation, Figure 16(c).

6 CONCLUSION

In this paper a flapping and flexible airfoil was investigated at low-Reynolds number flow conditions with the aid of coupling simulation environment. A laminar separation bubble occurs on the upper side of the airfoil, which moves during a flapping period along the airfoil. Therefore, laminar-turbulent transition prediction has to be taken into account as part of the fluid solver. A coupled steady state analysis was used to calculate the jig-shape of the airfoil to create a flexible model for wind tunnel test campaigns. Flapping flight simulations for specific testcase were compared with experimental data, which were conducted with the aid of stereoscopic PIV measurements. The comparison of experimental and numerical data has shown a good agreement. However, discrepancy has found in the rate of transition location change and the trailing edge deformation.

Further, parameters studies were systematically made, with the goal to improve the propulsive efficiency. A better flapping flight efficiency could be found, when the plunging amplitude is increased, but only to a certain value, when no leading edge separation occurs. More flexible airfoils reduce the propulsive efficiency. However, with the aid of a temporal adaptive stiffness of the airfoil (more stiff during downstroke, more flexible during the upstroke), an improvement of the efficiency could be noticed.

REFERENCES

[1] J. Windte and R. Radespiel. Propulsive efficiency of a moving airfoil at transitional low reynolds numbers. *AIAA Journal*, 46(9):2165–2177, 2008.

[2] T.J. Mueller. *Fixed and Flapping Wing Aerodynamics for Micro Air Vehicle Applications.* AIAA, 2002.

[3] M. Ol. Comparison of laminar separation bubble measurements on a low reynolds number airfoil in three facilities. *AIAA-Paper 2005-5149*, 2005.

[4] S. Heathcote and I. Gursul. Flexible flapping airfoil propulsion at low reynolds numbers. 45(5):1066–1079, 2007.

[5] Y. Lian and W. Shyy. Laminar-Turbulent transition of a low reynolds number rigid or flexible airfoil. *AIAA Journal*, 45(7):1501–1513, 2007.

[6] W. Yuan, M. Khalid, J. Windte, U. Scholz, and R. Radespiel. Computational and experimental investigations of low-Reynolds-number flows past an aerofoil. *The aeronautical journal*, 111(1115):17–30, 2007.

[7] R. Radespiel, J. Windte, and U. Scholz. Numerical and experimental flow analysis of moving airfoils with laminar separation bubbles. *AIAA Journal*, 45(6):1346–1356, 2007.

[8] O. Marxen, U. Rist, and S. Wagner. Effect of Spanwise-Modulated disturbances on transition in a separated boundary layer. 42(5):937–944, 2004.

[9] R. Unger, M.C. Haupt, and P. Horst. Coupling techniques for computational non-linear transient aeroelasticity. *Proceedings of the Institution of Mechanical Engineers, Part G: Journal of Aerospace Engineering*, 222(4):435–448, 2008.

[10] M. Haupt, R. Niesner, R. Unger, and P. Horst. Coupling techniques for thermal and mechanical Fluid-Structure-Interactions in aeronautics. *PAMM*, 5(1):19–22, 2005.

[11] K.J. Bathe. *Finite element procedures*. Prentice Hall, 1996.

[12] O.C. Zienkiewicz and R.L. Taylor. *The finite element method for solid and structural mechanics*. Elsevier Butterworth-Heinemann, Amsterdam, 6th ed. edition, 2005.

[13] R. Unger, M.C. Haupt, P. Horst, and J. Windte. Structural design and aeroelastic analysis of an oscillating airfoil for flapping wing propulsion. *AIAA-Paper 2008-306*, 2008.

[14] N. Kroll. MEGAFLOW - a numerical flow simulation tool for transport aircraft design. *ICAS-Paper 2002-1105*, 2002.

[15] G. Schrauf. LILO 2.1 user's guide and tutorial. Technical Report GSSC Technical Report 6, Bremen, 2006.

[16] A.M.O. Smith and N. Gamberoni. Transition, pressure gradient, and stability theory. Technical Report ES 26 388, Douglas Aircraft, El Segunda, California, 1956.

[17] J.L.van Ingen. eN method for transition prediction: Historical review of work at TU delft. *AIAA-Paper 2008-3830*, 2008.

[18] G. Schrauf. An inverse rayleigh iteration for complex band matrices. *ACM Transactions on Mathematical Software*, 17(3):335340, 1991.

[19] R. Unger, M.C. Haupt, and P. Horst. Application of lagrange multipliers for coupled problems in fluid and structural interactions. *Computers & Structures*, 85(11-14):796–809, 2007.

[20] S. Piperno. Explicit/implicit fluid/structure staggered procedures with a structural predictor and fluid subcycling for 2D inviscid aeroelastic simulations. *International Journal For Numerical Methods In Fluids*, 25(10):1207–1226, 1997.

[21] S. Bansmer, R. Radespiel, R. Unger, M. Haupt, and P. Horst. Validations of numerical schemes to predict propulsive efficiencies of rigid and flexible flapping airfoils. *AIAA Journal*, 0(0):0–0, 2010.

[22] H.G. Kuessner. Zusammenfassender Bericht ueber den instationaeren Auftrieb von Fluegeln. *Luftfahrtforschung*, 13:410–424, 1936.

[23] O. Lilienthal and G. Lilienthal. *Der Vogelflug als Grundlage der Fliegerkunst - Ein Beitrag zur Systematik der Flugtechnik*. R. Gartners Verlagsbuchhandlung, Berlin, 1889.